

Hydrodynamic pumping by serial gill arrays in the mayfly nymph *Centroptilum triangulifer*

Andrew T. Sensenig^{1,*}, Ken T. Kiger² and Jeffrey W. Shultz¹

¹Department of Entomology, University of Maryland, College Park, MD 20742, USA and ²Department of Mechanical Engineering, University of Maryland, College Park, MD 20742, USA

*Author for correspondence at present address: Department of Biology, University of Akron, OH 44325, USA (andrew6@uakron.edu)

Accepted 26 May 2010

SUMMARY

Aquatic nymphs of the mayfly *Centroptilum triangulifer* produce ventilatory flow using a serial array of seven abdominal gill pairs that operates across a Reynolds numbers (Re) range from 2 to 22 during ontogeny. Net flow in small animals is directed ventrally and essentially parallel to the stroke plane (i.e. rowing), but net flow in large animals is directed dorsally and essentially transverse to the stroke plane (i.e. flapping). Detailed flow measurements based on Particle Image Velocimetry (PIV) ensemble-correlation analysis revealed that the phasing of the gills produces a time-dependent array of vortices associated with a net ventilatory current, a fluid kinematic pattern, here termed a ‘phased vortex pump’. Absolute size of vortices does not change with increasing animal size or Re , and thus the vortex radius (R_v) decreases relative to inter-gill distance (L_{is}) during mayfly growth. Given that effective flapping in appendage-array animals requires organized flow between adjacent appendages, we hypothesize that rowing should be favored when $L_{is}/R_v < 1$ and flapping should be favored when $L_{is}/R_v > 1$. Significantly, the rowing-to-flapping transition in *Centroptilum* occurs at $Re \sim 5$, when the mean dynamic inter-gill distance equals the vortex radius. This result suggests that the Re -based rowing–flapping demarcation observed in appendage-array aquatic organisms may be determined by the relative size of the propulsive mechanism and its self-generated vortices.

Supplementary material available online at <http://jeb.biologists.org/cgi/content/full/213/19/3319/DC1>

Key words: intermediate, Reynolds number, rowing, flapping, aquatic, larvae, insects.

INTRODUCTION

Animals vary in the number, arrangement and kinematics of the appendages they use to generate flows for propulsion, ventilation or feeding, but comparative studies have revealed a fundamental relationship between the dynamic scale of such systems, as captured by the well-known Reynolds number (Re), and patterns of appendicular movement. Specifically, stroke kinematics can be broadly divided into flapping (where net flow or thrust is largely perpendicular to the stroke) and rowing (where net flow occurs largely parallel to the stroke), with flapping found to occur when $Re > 100$ and rowing predominating at lower Re (Walker, 2002). The discovery of an association between behavior and the extremes of the Re range is significant, but detailed studies of well-chosen systems are needed to understand how this association is actually manifested as flow around and between appendages and, ultimately, why flapping or rowing should be favored within a particular range of Re . Progress has been hampered by the paucity of animal models that use a single set of appendages to transit the relevant Re spectrum (i.e. 1–100). Most organisms studied thus far either occupy one side of this spectrum or use morphologically distinct mechanisms on either side, such as cilia or wing-like flaps in Antarctic pteropods (Childress and Dudley, 2004) and antennae or legs in some crustaceans (Williams, 1994b).

Here we provide a detailed Particle Image Velocimetry (PIV)-based analysis of the gill array of nymphs of the mayfly *Centroptilum triangulifer* (McDunnough) (Ephemeroptera: Baetidae). The ventilatory system of *C. triangulifer* has several desirable properties that facilitate analysis over the many described free-swimming

crustacean appendage systems (Hunt et al., 2007; Jiang et al., 2002; Kohlhage and Yager, 1994; Lent, 1977; Malkiel et al., 2003; van Duren and Videler, 2003; Williams, 1994a). The gills shift from a rowing- to flapping-type stroke while transiting a fairly narrow range of $4 < Re < 9$ during growth, which itself spans from $2 < Re < 22$ over their typical life cycle (Sensenig et al., 2009). The animal naturally rests on the substratum while beating its gills at high frequencies (20–50 Hz), which allows fine-scale tracking of generated flow and vorticity *via* analysis of high-speed video and ensemble-correlation techniques. Previous measurements of foraging and locomoting copepods (Jiang et al., 2002; Malkiel et al., 2003; van Duren and Videler, 2003) and krill (Yen et al., 2003) used multi-planar time-averaged velocity fields or sparsely seeded digital holography (Jiang et al., 2002; Malkiel et al., 2003) to describe the time-average velocity field around the appendage set, but these approaches did not resolve fluid motion between appendages. Our methods offer unprecedented resolution of flow through an array of moving appendages that operate at intermediate Re and allow visualization of both transient, local flow and time-averaged, far-field flow.

Our results indicate that flow within the mayfly gill array at all sizes is produced by ring vortices generated at the margins of each moving gill, and that the metachronal phasing of the gill kinematics produces a time-dependent array of vortices that we term a ‘phased vortex pump’. Gill oscillation frequency and mean vortex radius did not change as animal size and Re increased during growth; that is, the approximately constant oscillation frequency resulted in a similar diffusion time for vorticity generated by the plates and hence similar diffusion lengths throughout ontogeny. Consequently, at

small ‘rowing’ sizes ($Re < \sim 5$), the gill array produces relatively large vortices that span one or more inter-gill spaces, with dorsal and ventral vortices acting as a coordinated dipole pair during the powerstroke. Vortices at this scale effectively occlude the inter-gill space, and any vortically induced flow would occur longitudinally and in parallel with the rowing stroke plane. However, at larger ‘flapping’ sizes ($Re > \sim 5$), vortices are proportionally smaller and do not consistently span inter-gill spaces. The rowing-to-flapping transition in *Centropilum* occurs at $Re \sim 5$, when the ratio of mean dynamic inter-gill distance to vortex radius is approximately 1.

MATERIALS AND METHODS

Nymph preparation

Centropilum triangulifer is a multi-voltine mayfly of eastern North America (Funk et al., 2006). Most nymphs in this study were derived from a stock population (Stroud Water Research Center, Avondale, PA, USA), and reared from eggs at 20°C in about 1 cm of water

within covered Petri dishes. The water was a mixture of distilled and stream water (White Clay Creek, Avondale, PA, USA), and the stream water contained the nymph’s primary food of diatoms and other microbial debris. The shallow water precluded the need for an aerator, and a few hours of sunlight was sufficient to maintain the diatoms. Nymphs developed a bilateral pair of gill plates on seven adjacent abdominal segments at animal body lengths of about 1 mm. The gill plates enlarged and oscillated more often as nymphs grew to a maximal length of about 6 mm. Nymphs were also captured in Paint Branch Creek, College Park, MD, USA, periodically throughout the year. Ventilation flow could be observed using a dissecting microscope as nymphs crawled and fed on detritus in the Petri dish. The flow around the array could be deduced qualitatively from the motion of suspended detritus and numerous single-celled organisms that were entrained in the ventilation current during periodic activation of the array. Live nymphs were prepared for quantitative flow imaging by mounting in a clear glass chamber

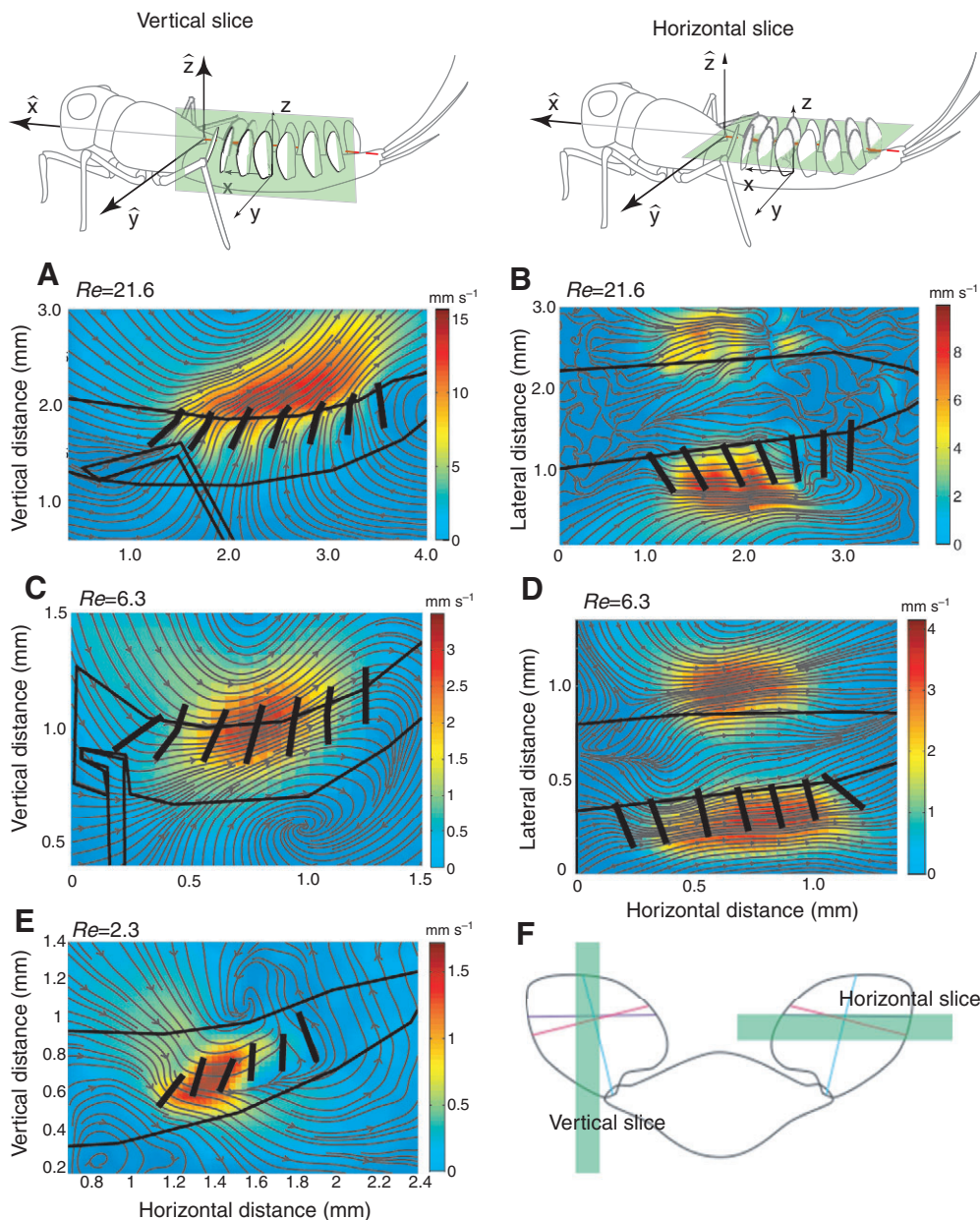


Fig. 1. Mean vertical and horizontal flow field at selected Re s (streamlines with background colored by velocity magnitude). The drawings above depict the region around the abdomen, with the thorax and head to the left (out of the field of view) and the caudal filaments to the right. Bold black lines indicate the body outline, mean gill positions, and any legs in the field of view. (A) vertical slice, $Re = 21.6$; (B) horizontal slice, $Re = 21.6$; (C) vertical slice, $Re = 6.3$; (D) horizontal slice, $Re = 6.3$, and (E) vertical slice, $Re = 2.3$. (F) The location and thickness of the vertical and horizontal laser light sheets are indicated in the transverse plane. The abdomen cross section and paired gill plates are shown in outline, with span, distal hinge and chord shown as blue, purple and magenta lines, respectively.

using a small pin (Sensenig et al., 2009). The temperature of the water in the chamber was recorded by periodic measurement with a digital thermometer, and was between 20 and 25°C.

PIV implementation and gill tracking

Images of the vertical plane were captured by intersecting the laser light sheet (described below) with one side of the gill array as the animal was moved laterally into the sheet using a micromanipulator (Fig. 1A,C,E,F). The location of the light sheet was centered between the lateral and medial extent of the gill plates (± 0.2 mm), as indicated schematically in Fig. 1F. Horizontal plane images were generated with a light sheet that intersected the gills at the hinge line on both left and right sides, with this slice illustrated in Fig. 1B,D,F. We present data from horizontal planes of four individuals, and from vertical planes of 12 individuals (Table 1). Laser power was minimized during focusing and completely blocked when not needed, and maximized to 2 W during movie capture, which lasted several seconds. Three-dimensional kinematics derived from diffuse white lighting and PIV slices derived from laser illumination were compared for the same individual and revealed that the brief exposure to the laser did not significantly affect kinematics. Motion in the horizontal plane was not measured using PIV at scales of $Re < 6$, but was instead observed qualitatively in full volume white (non-laser) light in both restrained and unrestrained nymphs.

Planar cinematographic PIV (1000 frames^{-1} ; exposure time $950 \mu\text{s}$) was conducted using a high-resolution CMOS imager (Phantom v9, 1632×1200 pixels). The field of view during maximum magnification of the Leica dissecting microscope was $3 \text{ mm} \times 3 \text{ mm}$, and this was used for the smallest nymphs. A field of view extending up to $9 \text{ mm} \times 9 \text{ mm}$ was used for the largest nymphs. A ruler with millimeter markings was mounted in an identical aquatic chamber and photographed at each magnification used. A 400-mm (focal length) plan-convex lens and 63-mm (focal length) plan-cylindrical lens was used to generate a light sheet from the beam of a continuous Argon ion laser (maximum power 2 W; Coherent Innova 90, Santa Clara, CA, USA). The light sheet was approximately 20 mm wide and 0.15 mm thick at the location of imaging. The light sheet was measured by placing 'burn paper' on the measurement stage, and then measuring the width of the burn with a dissecting microscope. Although this means of measurement is dependent on the sensitivity of the paper, which was not

quantified, our practical experience at lower power levels suggests that this measure is probably indicative of a width that reflects 90% of the beam's energy. Estimation of the depth of correlation provided by our imaging optics (Olsen et al., 2000) is approximately 0.17 mm, which indicates that the illuminated sheet thickness effectively defines the measurement volume. Hollow glass beads ($11\text{-}\mu\text{m}$ mean diameter; Grade 110P8; Potters Industries, Malvern, PA, USA) were added to the water as seeding particles, and needed to be periodically stirred to resuspend and remove them from the glass walls.

Framing rates of 1 kHz allowed for cyclical resolution of approximately 10 deg, with a spatial resolution of approximately $25 \mu\text{m}$ for a 3-mm field of view. This level of resolution is possible through the use of ensemble-correlation PIV (Meinhart et al., 2000), as the cyclic flow is ostensibly laminar and highly repeatable from cycle to cycle. Ensemble-correlation PIV uses multiple frame pairs from approximately the same stroke phase to average the correlation before vector computation. Because the imaging frequency was not an exact multiple of each animal's oscillation frequency, care had to be exercised to ensure that a proper set of image frames was used to construct the ensemble. This was done by selecting an initial representative frame from the beginning of the sequence, and then searching for the best match among the possible frames that were expected to match, based on the cycle frequency of the animal. The quality of the match was determined by cross-correlation of the gill-plate locations within each frame. Of the approximately 30 cycles recorded in a typical imaging sequence, an ensemble of $N=10$ frame pairs was found to be sufficient to converge velocity fields at the desired resolution, providing a close match within each frame. The influence of light scattered by the gill plate was removed by subtracting the mean image for the local ensemble prior to computation of the correlation. The size of the initial sub-image for the ensemble-correlation PIV procedure was 128 pixels, and reduced to 32 for the second and final correlation. Overlap between sub-images was 50%. The vector field was then conditioned during both the intermediate and final passes using the standard median filter technique with an iterative replacement of any rejected vector from secondary peaks within the cross-correlation. The mean velocity field over a complete stroke was computed by averaging the velocity at each point in the two-dimensional space over all frames in the cycle (varied between 21–49 frames). Assuming a conservative estimate of the sub-pixel displacement accuracy of 0.1 pixels, an

Table 1. Fluid kinematic parameters of nymphs

L_g (mm)	Gill 2–6 root separation (mm)	Water temperature (°C)	Vertical imaging						Horizontal imaging
			f (Hz)	η	Re_f	Dorsal vortex p:r circulation ratio	Vortex 4 max area (mm^2)	Vortex max radius gill 4 (mm)	f (Hz)
0.30–0.32	0.57	20	19–21	1.0	1.8–2.1	–0.33	0.040	0.23	
0.21–0.23	0.48	25	47–49	0.9	2.3–2.6	–0.60	0.026	0.18	
0.37–0.41	0.66	25	32–34	0.9	5–5.9	–0.42	0.108	0.37	33
0.45	0.69	25	30	0.9	6.8	–0.42	0.072	0.30	
0.47	0.68	20	29	1.0	6.4	–0.32	0.066	0.29	
0.51	0.65	20	24	1.0	6.2	–0.55	0.066	0.29	
0.58	0.79	20	21	1.0	7.1	–0.50	0.055	0.26	21
0.65	0.70	20	26	1.0	11.0	–0.62	0.073	0.31	
0.65	0.70	20	19	1.0	8.0	–0.62	0.073	0.31	
0.70	1.05	20	33	1.0	16.2	–0.76	0.038	0.22	
0.82	1.28	20	30	1.0	20.2	–1.02	0.054	0.26	29
0.77–0.80	1.50	20	34	1.0	20.2–21.6	–0.91	0.077	0.31	29

Nymphs are listed approximately in order of increasing size and developmental age (where available), with growth over about 30 days represented in the table.

For several very small and one large individual, a range of Re_f is reported, representing error derived from repeated measures of gill length and frequency.

interframe time of 1 ms, and a image resolution of $25 \mu\text{m pixel}^{-1}$, the maximum uncertainty for the velocity was taken to be 2.5 mm s^{-1} , which was typically 5–10% of the maximum velocity.

To map the gill positions onto the velocity field derived from ensemble correlation, the gill positions within the mean image for the local ensemble was digitized using MatLab 7.0 (MathWorks, Inc., Natick, MA, USA) by manually indicating the abdomen, legs and ventral gill location, within-gill hinge point and dorsal gill tip. The raw gill plate points were then smoothed in space and time using a cubic spline fit (Matlab 7.0, ‘smooth’). Smoothing altered any individual point position by less than 10% of the gill length.

Hydrodynamic definitions

One of the most important hydrodynamic parameters in the study of oscillatory pumping or locomotion is the Reynolds number (Re), which relates the relative roles of inertia and viscosity in the governing dynamics through the definition $Re=LU/\eta$, where L is the characteristic length of the appendage or moving body, U is the characteristic velocity, and η is the kinematic viscosity. For the case of propulsion, U is typically taken to be that of the forward motion of the body being propelled, and the oscillatory nature of the appendages is introduced through the parameter of the advance ratio or reduced frequency, $k=fL/U$. For hovering flight, or stationary pumping as in the case of mayfly nymphs, the standard definition for Re becomes equal to zero, while the reduced frequency becomes infinite. In this case, it is more common to reformulate the characteristic velocity as being proportional to the appendage oscillation frequency and span length, thereby giving a new definition of an oscillatory Re number, $Re_f=fL_g^2\eta^{-1}$. This can also be seen as equivalent to the product of the Re number and the reduced frequency. In the current work, we took our characteristic length from the gill span in mm (L_g), the oscillation frequency in Hz (f) and kinematic viscosity in cSt (η), as adopted in similar works (Borrell et al., 2005). Note that Re_f gives a value that is proportional, but not equivalent to, the maximum tip Re number. The exact proportionality would be altered by specific values of the stroke angle range, the duty cycle and asymmetries between the protraction and retraction stroke, and a factor of 2π .

Calculation of vorticity and circulation

Vorticity is a useful construct in which to study unsteady flows because of its connection to the fluid kinematics and its capacity to estimate the dynamic load on an immersed body independent of a mechanistic model. Vorticity descriptions have proved useful for bird wakes (Rayner, 1979; Spedding et al., 2003), fish (Drucker and Lauder, 1999) and insects (Ellington, 1984; Poelma et al., 2006). In particular, for situations where the vorticity is compact and distinctly organized, it can offer a potentially simpler and more convenient means for direct calculation of unsteady hydrodynamic forces (Wu, 1981). It should be pointed out, however, that in order for quantitative unsteady loading information to be calculated, the velocity field should have adequate spatial and temporal resolution as well as provide a complete description of local vorticity distribution. In the current measurements, the temporal and spatial resolution conditions are probably adequate, however, our measurements represent only a two-dimensional slice from a complex three-dimensional flow field, and hence would probably produce inaccurate results for the unsteady forces.

Here, vorticity was calculated using a second order central difference approximation (Matlab R2007b ‘curl’ function) on the validated (median filtered with iterative replacement of outlier vectors as noted above) velocity field data. Individual vortices

adjacent to the gill plates were identified within each frame as spatial regions where vorticity exceeded 25% of the peak value observed during the complete cycle (Poelma et al., 2006). If a given vortex appeared to span more than a single gill, the identified region was segmented into smaller zones that were assigned to the closest appendage. Often, such vortices appeared to exhibit a narrowing or ‘pinching’ between the gills, suggesting a boundary where the originally distinct vortices produced by adjacent gill plates were diffusing into a single structure (Fig. 3, DP2– and DP3–; DP, dorsal protraction vortex). Such features provided a natural demarcation to guide the segmentation. This was almost always the case for merging vortices in the high Re conditions, but owing to increased diffusion at the low Re , such points were not readily visible (e.g. Fig. 2, DP2–). In these low Re cases, the vortex was segmented geometrically by simply assigning regions based on proximity to a given gill plate. This merging of vortices at low Re can be explained by the fact that although viscous diffusion rate is similar for all nymphs in water with fixed viscosity, vorticity for the small nymphs diffuses a greater percentage of a gill length in a given time interval, because of the smaller spacing between gills and use of an oscillation frequency similar to that of the larger nymphs.

Once segmented, the circulation (Γ) of a given vortex region was calculated using its definition:

$$\Gamma = \oint \omega \cdot \mathbf{n} dA, \quad (1)$$

which is the area integral of the vorticity that is within the specified domain (ω is the vorticity vector, \mathbf{n} is the unit normal vector for the surface of integration, and dA is the scalar differential area of the surface). In our case, the flow fields are extracted in two-dimensional planes, and so the measured vorticity component is always the one normal to the observation plane. In practice, the circulation of a vortex was approximated by summing the vorticity within the given region and multiplying by the vector spacing squared. For those cases where the vorticity spanned multiple gills over multiple frames, the total circulation of the vortex was calculated and compared with the per-gill ‘segmented’ values. The peak circulation of a gill-specific segmented vortex was about 15% less than the circulation of its associated non-segmented ‘total’ vortex. Circulation values

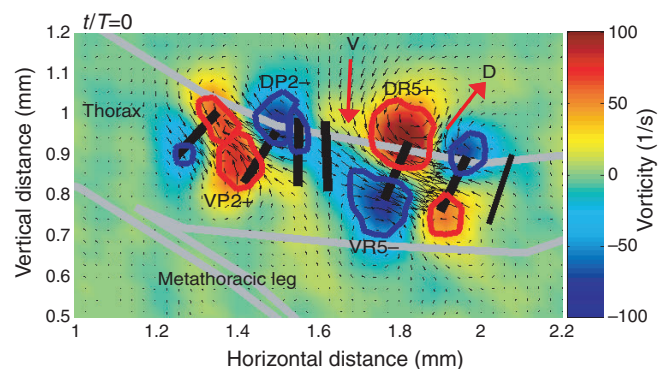


Fig. 2. Instantaneous vorticity and velocity field within a vertical slice at phase $t/T=0$ for a small nymph $Re_f=2.6$. Each posterior gill leads its anterior neighbor by approximately $1/4$ cycle. Individual vortices are named according to their dorsal (D) or ventral (V) position, protraction (P) or retraction (R) phase, and clockwise (–) or counterclockwise (+) vorticity. Ventral induced flow (V) moves into intergill space 4 as gill 5 retracts. The magnitude of dorsal induced flow (D) associated with intergill space 5 is much lower than the magnitude of V, partially explaining the net ventral flow over a full stroke cycle. The solid red and blue lines indicate the isovalue of 25% of the peak vorticity magnitude, and are used to indicate the general boundary of the identified vortices.

were non-dimensionalized by dividing by gill length and by the square of the gill oscillation frequency, in order to facilitate comparison between nymphs of different sizes (Fig. 6). Non-dimensional circulation was calculated as $\Gamma/(L_g^2 f)$.

Calculation of inter-gill sectional flux

The net flow produced by a given set of stroke kinematics is a useful metric to compare the local contribution to the overall flow and the phase dependence of the flow. For the case of a serial array of appendages, we determined the phase-dependent flux produced by a set of two longitudinally adjacent gills, termed inter-gill flux. This flux through the inter-gill plate spaces was quantified by calculating the net flux across three distinct line segments (dorsal, mid-gill and ventral) in the vertical perspective. These three line segments were demarcated by a line connecting two homologous locations on adjacent plates at each instant in time: (1) the uppermost (dorsal) extent of the gill plate, (2) the hinge flexion points (mid-gill) visible from the motion of the plates, and (3) the lowermost (ventral) extent of the gill plate (Fig. 3). For animals not having a distinct hinge point, the flow through the mid inter-gill space was defined by a line between the mid-point of the root–tip line. The two-dimensional flow across these lines was quantified by averaging the component of the velocity vectors projected normal to that line. Dorsally directed flow was assigned to be positive, and ventral negative.

$$\Delta Q = (\mathbf{v} \cdot \mathbf{n}) \Delta l, \quad (2)$$

where ΔQ is the local flux, \mathbf{v} is the velocity vector, \mathbf{n} is the outward-pointing unit normal vector of the control volume, and Δl is the scalar incremental length along the line. Flux values were non-dimensionalized by the square of the gill length and the oscillation frequency, to enable comparison between different sized instars and different frequencies. Uncertainty in measurements of inter-gill flux and circulation was estimated by the standard deviation of this parameter across typical inter-gill spaces of 2, 3, 4 and 5 ($N=4$; Fig. 7). Variation of these parameters across gill plates within a single animal could occur as a result of error in aligning the light sheet parallel to the animal's abdomen, different kinematic amplitude of

each plate, and different plate shapes. All of this variation would be captured by the standard deviation across gill plates within a single animal.

Although inter-gill flux was the average across the line at a specific phase, time-averaged inter-gill flux was the average across the full stroke cycle. Both the inter-gill flux and the time-averaged inter-gill flux through the dorsal, mid-gill, and ventral line segments should be equal in two-dimensional flow. Our measured deviation from this indicated the three-dimensional nature of the gill-plate ventilation current. Specifically, time-averaged outflux through the dorsal line ranged from 30 to 70% higher than the influx through the ventral line for the ontogenetic stages of $Re_f > 10$, but was more similar in magnitude for the two lowest Re_f cases.

Statistical treatment of flow parameters

The similarity of the flow between adjacent gill spaces enabled construction of an average vorticity and flux behavior as a function of phase within each animal, by adjusting fluid and gill kinematics to a common stroke period. A dimensionless time $\tau = t/T$ was defined as the fraction of a stroke period, with the arbitrary definition of $\tau=0$ taken to be in the initiation of retraction of gill 4. The kinematic pattern of each gill was phase delayed with respect to its posterior neighbor, and therefore the flow features (flux through defined lines, vortices) were similarly shifted. The phase lag was measured to be $0.20 < \Delta\tau < 0.25$, such that gills 2 and 6 were in equivalent phases of a stroke at any given time. Amplitudes of the kinematics and flow features were lower for edge gills of the array. Gill 1 was located at the anterior edge of the array, while gill 6 represented the posterior edge of the mobile gills, as gill 7 was always stationary. The time-averaged flow through inter-gill spaces 1–2 and 6–7 were always much reduced compared with the others (Fig. 1), potentially because of both the lower kinematic amplitude and boundary effects. In order to summarize the basic fluid dynamic operation of the typical center gill plates, the instantaneous flux and circulation values were ensemble averaged within each animal across gills 2, 3, 4 and 5. In order to facilitate the ensemble average among adjacent gill plates, the instantaneous circulation and flux associated with each gill was phase adjusted so that the retraction–protraction phases were standardized to have a time $\tau=0$ defined by the initiation of retraction of the respective gill (Fig. 6A, Fig. 7).

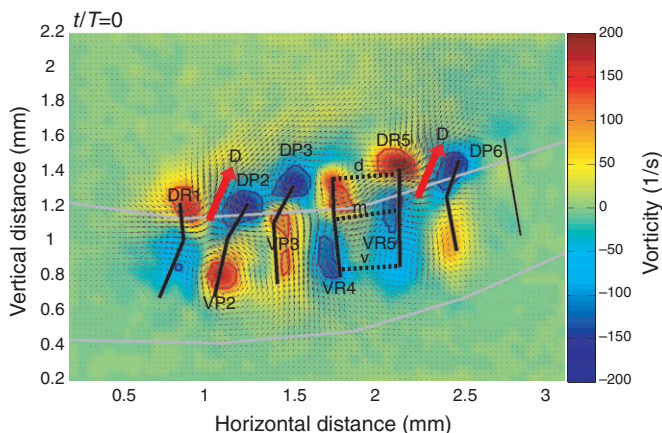


Fig. 3. Instantaneous vorticity and velocity field within a vertical slice at phase $t/T=0$ for a large nymph $Re_f=20.1$. Individual vortices indicated by their dorsal or ventral position and protraction or retraction phase. Important fluid jet indicated by large arrows. Gill 4 has just begun retraction and is generating a new vortex (VR4) at its ventral edge. The flow in the intergill space 1 is approximately in phase with that through intergill space 5, producing a dorsal jet (D) from both spaces. Representative lines through which intergill flux was tracked are shown as dashed lines for intergill space 4 and labeled d (dorsal), m (middle) and v (ventral).

RESULTS

General observations and steady flow field

Mayfly nymphs of *Centroptilum triangulifer* grew gill buds at about 1 mm body length, and started oscillating the gill plates when at about 2 mm body length, corresponding to a gill length of about 0.2 mm. Gills oscillated at frequencies ranging from 20 to 50 Hz across all animal sizes, which in early instars corresponded to a Re_f of ~ 1 and for late instars to a Re_f of ~ 22 . For the smallest nymphs, protraction (the return stroke) consisted of rapid metachronal onset of gill movements and an asymmetry in the protraction speed, giving the overall effect of a near-synchronous protraction. For the largest nymphs, the protraction and retraction of each gill was offset by a consistent phase separation from the adjacent gill. Quantitative measurements were made for select individuals using PIV. Nymphs grew to about 6 mm body length, with 1 mm long gills. Nymphs < 3 mm long are hereafter typically denoted as ‘small’ nymphs, those > 4 mm as ‘large’ nymphs, and those 3–4 mm as ‘intermediate’ nymphs.

For the small instars (body size less than 3 mm, $Re_f < 5$), the entrained ventilation current consisted of a slow movement of water from the region dorsal to the head toward the array (Fig. 1E). Flow

several gill lengths above the abdomen (1 mm away) was about 0.5 mm s^{-1} . Upon reaching the array, the fluid particles moved rapidly out the ventral and lateral sides of the array, reaching mean speeds of about 2 mm s^{-1} . Flow ended virtually instantaneously when the array stopped oscillating as a result of the relatively small influence of inertia.

Flow in the intermediate instars (3–4 mm in body length, $5 < Re_f < 10$) was oriented differently relative to the animal. Fluid was entrained equally from ventral and dorsal anterior regions of the fluid (Fig. 1C,D). In the large instars (body length 4 mm and larger, $Re_f > 10$), fluid was entrained from the ventral and lateral sides of the animal and ejected away from the array in two dorsal jets (Fig. 1A,B).

Unsteady flow structure

The general features of the unsteady flow are indicated in the representative snapshots of a complete array in Figs 2 and 3, and

sequences focused on a single gill in Figs 4 and 5 (also see supplementary material Movies 1 and 2). Vortices were named for their instantaneous location on the gill plate (D=dorsal or V=ventral in the vertical plane, and M=medial or L=lateral in the horizontal plane), the stroke direction (R=retraction or P=protraction), their associated gill number (1–6), and the sign of the vorticity component measured in that particular plane (+ or -). Common to each gill, and across the span of Re_f observed, a pair of counter-rotating vortices formed on opposite sides of the gill plate over each half-stroke. During retraction, this corresponded to a positive vortex on the dorsal edge (DR+) and a negative vortex on the ventral edge (VP-), which gradually strengthened until mid-stroke and then started to weaken as retraction ceased. Upon protraction, a similar pair of vortices were generated but with an associated change in sign of the vorticity (DP- and VP+, respectively). A similar vortex pair was observed during retraction and protraction in the horizontal plane (MR+/LR- during retraction and MP-/LP+ during

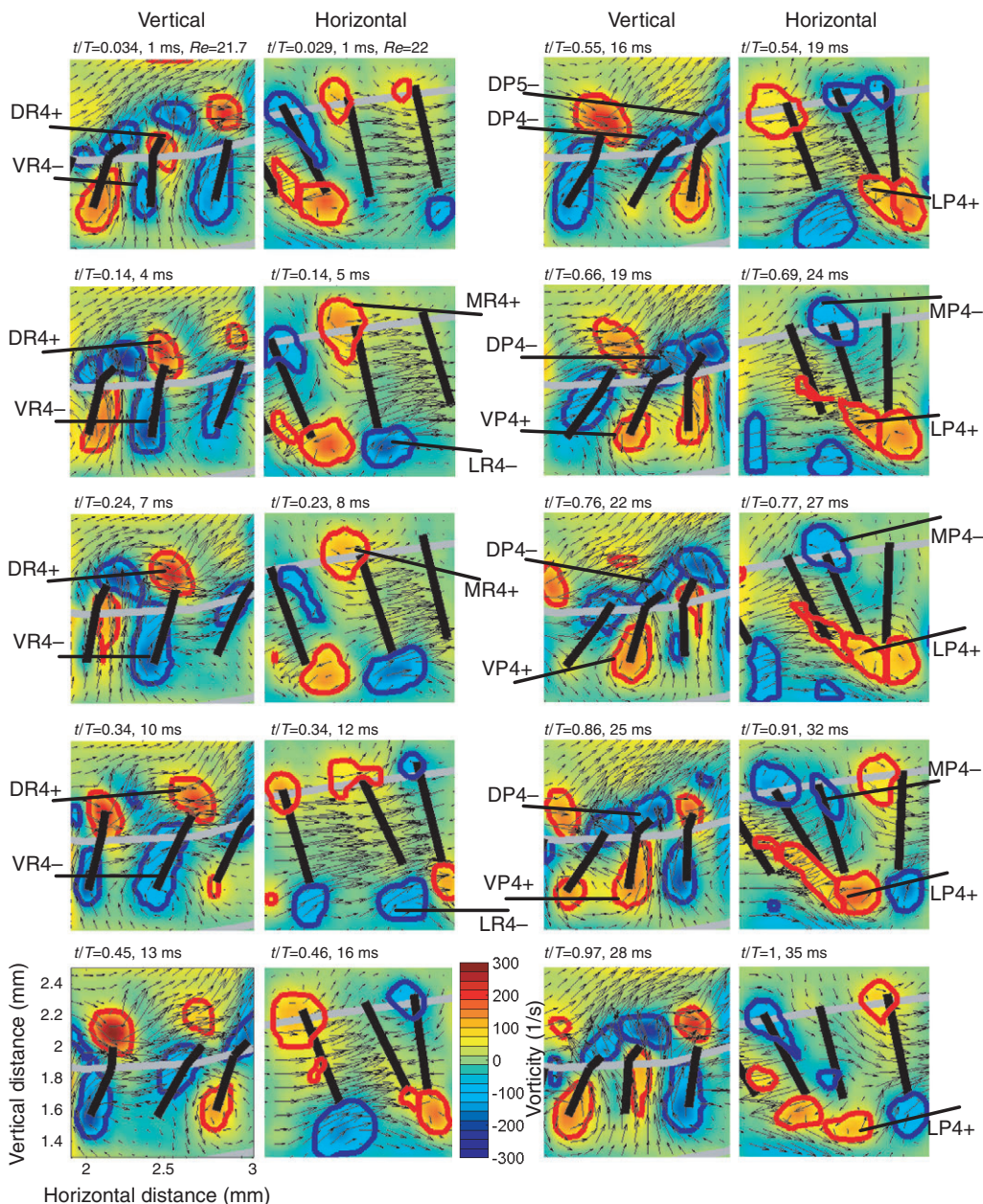


Fig. 4. Phase resolved flow at $Re_f = 21.6$. Vertical and horizontal plane images (left and right columns, respectively, of each double column) are shown at ~ 3 ms intervals, with the dimensionless time (t/T) also indicated for each frame. In both views, the head of the animal is toward the left, and the tail is toward the right. The gray line indicates the edge of the abdomen, and the heavy black lines depict the gill positions. The period was slightly longer (35 vs 29 ms) in the horizontal imaging of the array, because the animal changed frequency in the several minutes between image capture. The field of view is approximately centered on gill 4, but gill 3 and 5 are also visible in all frames.

protraction). The timing and arrangement of the vorticity sign between the horizontal and vertical measurement plane is completely consistent with the presence of a continuous vortex ring being produced on the outer edge of the gill boundary. The dissipation is comparatively high, even at the largest Re_f observed, resulting in a rapid decay of the vorticity once the gill half-stroke was complete. Vortex dissipation occurred rapidly relative to the stroke cycle so that structures ceased to exist between half-strokes, typically dissipating within 4 ms or $0.10 t/T$.

Fig. 4 follows gill 4 (center of the three gills shown) as a stereotypical central gill of the array, and highlights the features unique to the higher Re_f nymphs ($Re_f > 20$). In particular, distinct asymmetries in the vortex motion are clearly visible with a bias predominantly toward the dorsal side. On the ventral edge, the vortices are elongated along the gill surface by mid-stroke ($t/T=0.24$ for VR4- and $t/T=0.76$ for VP4+; VR, ventral retraction vortex), inducing a significant flow within the intergill space, and subsequently ending the half-stroke on the dorsal edge. The complementary dorsal vortex is observed to trail from the edge of the gill and extend into the flow region dorsal to the array, which is particularly noticeable upon protraction ($t/T=0.76$ for DP4-) where this vortex is brought into close proximity to a similar signed vortex on the immediately posterior gill (DP5-).

The imaging plane for the horizontal slice was approximately at the gill 4 plate hinge (Fig. 1F), and depicts a vortex structure consistent in sign and location that would indicate that a single vortex ring envelopes the circumference of the gill edge during each halfstroke. Near the end of retraction, vortex LR4- migrated laterally (time $t/T=0.34$), corresponding approximately to the dorsal shedding of DR4+ (Fig. 4; $t/T=0.45$). Therefore, the entire vortex loop was probably shed in the dorsolateral direction. During protraction, vortex LP4+ was generated in close proximity to the lateral edge of gill 5 ($0.46 < t/T < 0.69$), which corresponds closely to the behavior of the DP4-/DP5- vortices over the same time.

Evolution of the flow field typical of the smallest nymphs is depicted at eight phases of the stroke cycle in frames with only every fourth frame shown (Fig. 5). At time $t/T=0$, gill 4 was about to begin retraction while gill 5 was drawing fluid from the dorsal side into the widening inter-gill space between gill 4 and 5 ($t/T=0.02$; Fig. 2 flow region V; note that inter-gill space refers to space posterior to gill). As the gill plate 4 rapidly retracted (time $t/T=0.12-0.33$), large vortices were generated on both the dorsal (DR4+ vortex) and ventral (VR4- vortex) edges of the gill plate. During this phase, and particularly prominent near the end of this retraction, there was distinct downward flow on the ventral side of the gill 4 space (time $t/T=0.33$), and a smaller amount of upward flow on the dorsal side as fluid was squeezed out of the gill 4 space. For the small nymphs, the relatively large vortices associated with a gill plate were fused across several gills during protraction (Fig. 3, vortex DP2- fuses gill 2 and gill 3) but separated during retraction (e.g. Fig. 3, vortex DR5+ associated only with gill 5).

The vortex radius of *C. triangulifer* is constant during animal growth and thus becomes smaller relative to the gill array in later development. We measured this directly *via* observation of the maximum effective vortex radius during retraction ($R_v = (\text{vortex area}/\pi)^{0.5}$), with the vortex area defined as the region where the vorticity exceeded 25% of the cycle maximum value; Fig. 8), which was found to be nearly constant ($r^2=0.01$, $P=0.73$) as a function of Re_f . This is consistent with a diffusion-limited growth of the vortex rings associated with the stroke pumping. During each half-stroke, vorticity is generated at the surface of the gill by its relative motion, which subsequently is distributed by the combined action of

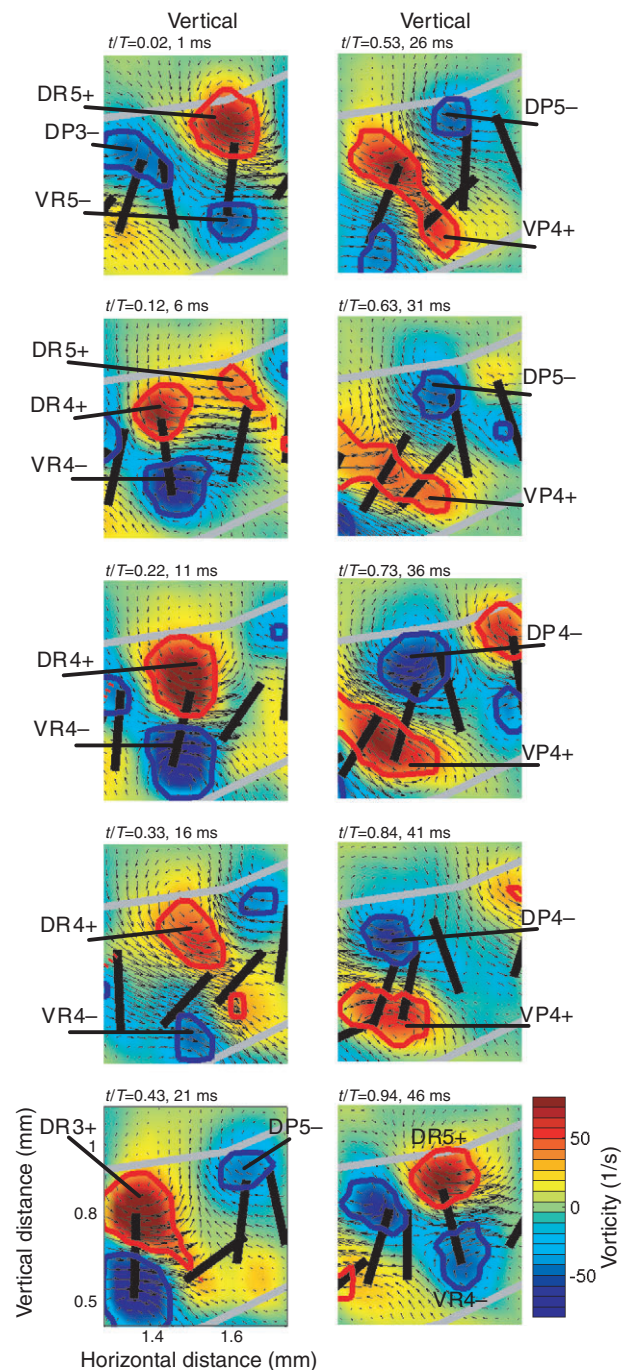


Fig. 5. Phase resolved vertical plane flow at $Re_f=2.3$. Only vertical flow imaging was possible for animals so small that $Re_f < 5$. The field of view is approximately centered on gill 4, but two gills on each side of gill 4 are visible in most frames.

convection and viscous diffusion into the observed vortex rings around the periphery of the gill plate. The physical extent to which the vorticity can spread (and hence the size to which a vortex can reasonably grow) is limited by the viscous diffusion length, which is proportional to $(\eta/f)^{0.5}$ and hence would be expected to be constant with ontogeny, given the invariance of the oscillation frequency with respect to Re_f and animal size (on average; Fig. 9B). Taking a mean frequency of 30 Hz, and a viscosity of $1 \text{ mm}^2 \text{ s}^{-1}$ gives an estimate of 0.18 mm, which is of similar magnitude to the observed value of 0.15 mm.

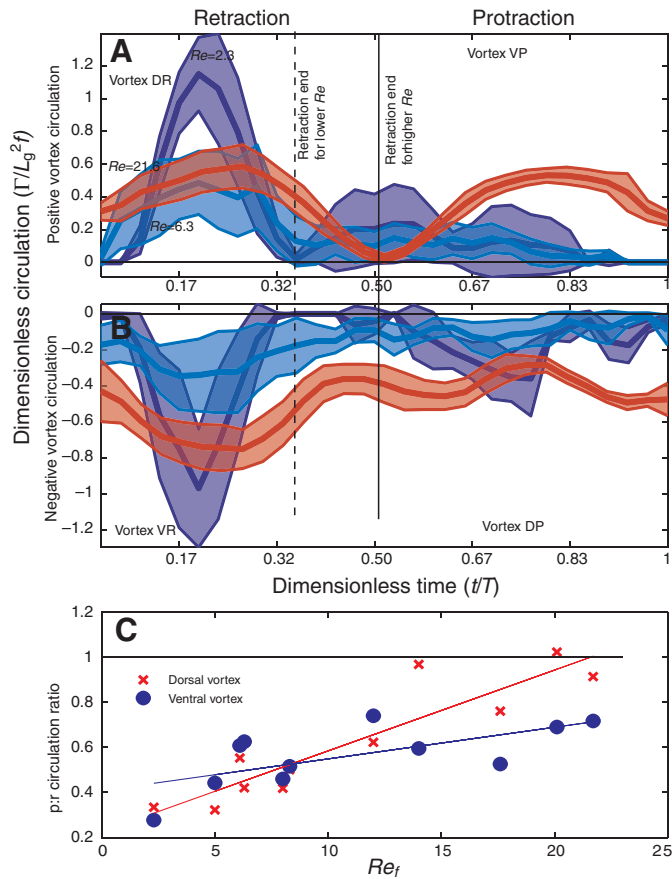


Fig. 6. (A,B) Vertical plane circulation history of positive and negative vortices ensemble-averaged across the central gills (2 to 5) of the array at three representative Re_f . Retraction occurs rapidly over about 0–0.35 t/T in the smaller nymphs, but over a longer time span of 0–0.5 t/T in the large nymphs. A normalized, dimensionless measure of circulation: $\Gamma/(L_g^2 f)$ – where Γ is circulation of the vortex, L_g is gill length, and f is plate oscillation frequency – is plotted for comparison of different-sized nymphs representing a 10-fold range in maximum absolute circulation (0.3–3 $\text{mm}^2 \text{s}^{-1}$). Curves denote the mean \pm 1 s.d. of gills 2, 3, 4, 5 ($N=4$). (C) Dorsal and ventral vortex protraction:retraction (p:r) circulation ratio as a function of Re_f . The p:r circulation ratio is the maximum circulation achieved by the vortex at the designated location during protraction divided by the maximum achieved during retraction. Rowing mechanics of the small nymphs are indicated by the lower p:r ratio.

Gill circulation history

As animals grew larger (and Re_f increased) the circulation ratio of the protraction:retraction (recovery:power) stroke increased, indicating higher symmetry. This trend was statistically significant for the dorsal vortex ($r^2=0.71$, $F_{1,10}=26$, $P<0.001$) but not for the ventral vortex ($r^2=0.20$, $F_{1,10}=2.5$, $P=0.14$; Fig. 6C). Circulation ratio of the protraction:retraction (recovery:power) probably increased partially because of the underlying kinematic speed ratio increase (Fig. 9A), since the measured degree of flexion of the gill plates did not correlate with the circulation ratio (Fig. 9C). A complete symmetry in vortex strength, however, was never achieved, even at the largest instars. For example, circulation of the vortex generated at the ventral edge of the gill during retraction (VR $t/T \sim 0.25$; Fig. 6B) was still about 30% higher at the higher Re_f than that generated at the ventral edge by protraction (VP $t/T=0.86$; Fig. 6A), giving a p:r ratio of 0.7 ($Re_f=21.6$). For the smallest animal, the standard deviation of the mean circulation of analogous vortices across gills

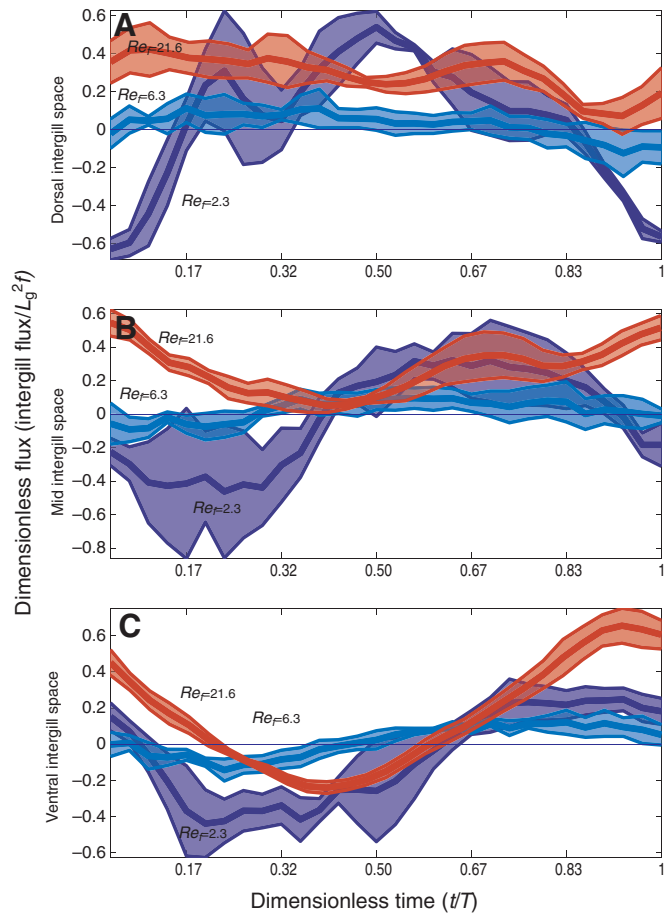


Fig. 7. (A–C) Vertical plane intergill flux history at three representative Re_f and through dorsal, mid and ventral apertures. The period was normalized to 30 ms for comparison. Retraction ranges between 1–15, and protraction ranges between 15–30 ms. A normalized, dimensionless value of flux: $\text{flux}/(L_g^2 f)$ – where flux is the flux through the intergill space, L_g is gill length, and f is plate oscillation frequency – is plotted for comparison of different-sized nymphs spanning a 14-fold range in maximum absolute intergill flux (0.45–6.2 $\text{mm}^2 \text{s}^{-1}$). The lower normalized intergill flux for the intermediate Re_f case ($Re_f=6.3$) may correlate with higher horizontal flow rates at this stage. Curves denote the mean \pm 1 s.d. of intergill spaces 2, 3, 4, 5 ($N=4$).

was 44% of the mean vorticity, whereas the standard deviation was 20% of the mean vorticity in the largest animal (Fig. 6A).

Inter-gill flux

For the high Re_f cases, the maximum inter-gill flow occurred during filling of the space across the ventral gap near the end of the stroke cycle ($0.8 < t/T < 1$; Fig. 7C). This corresponds to the ending of protraction of the anterior gill, and a mid-stroke retraction for the posterior gill, resulting in the drawing of fluid up into the widening gap. Similar, but weaker, maxima were found in the fluxes across the mid (Fig. 7B) and dorsal (Fig. 7C) section lines, but with weaker magnitudes, longer durations and with a slight phase delay relative to the ventral section. It should also be pointed out that the instantaneous flux is dorsally directed over almost the entire cycle at all sections, with the brief exception being a small regurgitation out the ventral edge near the end of the retraction ($t/T \sim 0.4$). For $Re_f < 3$, those phases of the stroke with downward flux through gill

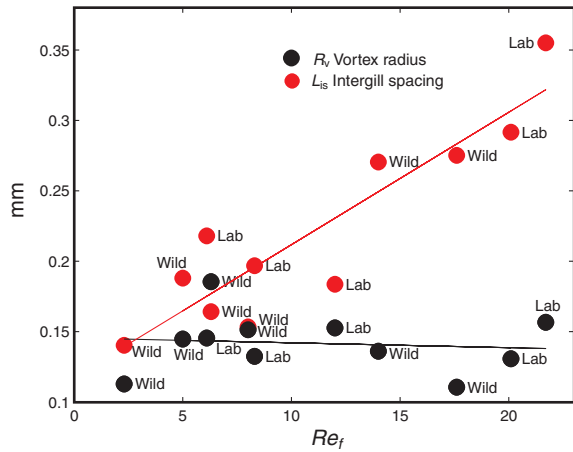


Fig. 8. Plot showing the relationship between vortex radius R_v and mean intergill spacing L_{is} . The hypothesis generated here maintains that the organized intergill flow required for effective flapping can only occur when the radius of self-generated vortices is $<L_{is}$. Significantly, R_v does not change absolute size during mayfly growth ($R^2=0.01$, $F=0.1$, $P=0.75$) but L_{is} increases ($R^2=0.82$, $F=41$, $P=0.0001$) and exceeds R_v at $Re \sim 6$. This value corresponds to the Re at which mayfly nymphs transition from rowing to flapping.

apertures (dorsal, d; mid, m; ventral, v; Fig. 3) were characterized by greater flux magnitudes over a shorter duration in comparison to the high Re_f case. For $Re_f < 3$, from time $0.85 < t/T < 1.15$ (Fig. 7A) the downward flow across the dorsal space was generated by retraction of the posterior gill, as the reference gill was itself undergoing minimal translation at that time. By mid retraction of the gill ($t/T=0.25$) however, the inter-gill space was reduced and resulted in an upward (+) flow out of this space (Fig. 7A; time $t/T=0.17-0.33$). As retraction completed ($0.15 < t/T < 0.5$), a downward flux from the ventral slot was generated. For the smallest animal, the standard deviation of the time-averaged inter-gill flux across gills was 250% of the mean time-averaged inter-gill flux, whereas

the standard deviation was only 25% of the mean time-averaged inter-gill flux in the largest animal (Fig. 7).

DISCUSSION

The goal of our study was to determine the hydrodynamic features associated with the rowing–flapping transition in the intermediate Re regime (i.e. $Re=1-100$). Interspecific comparisons of diverse animals have shown this transition to be nearly ubiquitous in biological fluid propulsion systems (Walker, 2002). The transition typically occurs as a significant ‘jump’ from one Re to another rather than as a series of incremental changes, and it often corresponds to a shift from the use of one set of propulsive structures to another. This pattern effectively precludes fine-scale correlation between gradual changes in flow structure and Re and is the principal motivation for focusing on the incremental growth of nymphal *Centroptilum triangulifer*. Our previous study of gill kinematics and gross ventilatory flow of *C. triangulifer* showed that the rowing–flapping transition occurs abruptly even in this organism that passes gradually through the relevant Re spectrum using a single set of appendages (Sensenig et al., 2009). In the present study, our measurements of incremental changes in the unsteady flow field highlight a key hydrodynamic role for ring vortices in determining the direction of net ventilatory flow across the range of observed Re as well as the Re at which the rowing–flapping transition occurs. Specifically, the effects of viscous diffusion and spatiotemporal manipulation by gill-plate kinematics progressively alter the relative size and distribution of ring vortices with increasing Re . The body size at which inter-gill spacing exceeds vortex radius corresponds to the Re at which organized inter-gill flow, and thus effective flapping, becomes possible.

Critical to understanding flow generation in *C. triangulifer* is how the vortices are arranged in space and time and how this arrangement varies with animal size and Re . Schematics of the vortex manipulation are shown for the extreme cases of $Re_f=21.6$ and 2.1 in Figs 10 and 11. Note that the static gill 7 is not shown in the figure, and that the non-dimensional cycle time of $t/T=0$ was arbitrarily set to the onset of retraction in gill 4 (shown in red). Starting with the high Re_f condition ($Re_f=21.6$; Fig. 10A), the regularity and synchrony of the

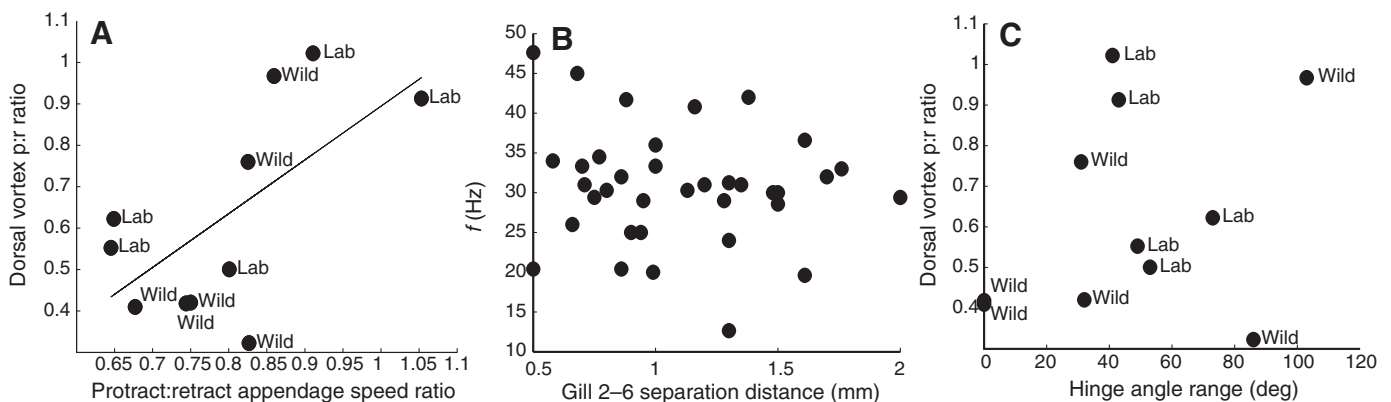


Fig. 9. (A) Appendage protraction:retraction speed ratio was correlated with dorsal vortex circulation protraction:retraction ratio ($R^2=0.40$, $F=6.09$, $P=0.035$). The dorsal protraction vortex was ‘segmented’ between only two gills for $Re \geq 18$, rather than among three gills as was the case for all smaller nymphs. (B) Gill plate oscillation frequency did not change with animal size, where animal size was measured as gill 2–6 root separation distance ($R^2=0.01$, $F=0.38$, $P=0.54$). Each point represents an individual animal. The data set represents an approximately equal sampling of wild and lab-reared nymphs. (C) Dorsal vortex p:r ratio was not correlated with gill hinge flexion ($R^2=0.09$, $F=0.86$, $P=0.37$). The two smallest nymphs had no measurable flexion in the hinge (two overlaid points on left side of graph). Intermediate and large nymphs had significant hinge flexion; in one individual up to 100 deg. Hinge flexion was measured here in the two-dimensional (2-D) vertical slice of the PIV images, which underestimated the true (3-D) hinge flexion by 25–40% (Sensenig et al., 2009). The 2-D estimate was used here because 3-D kinematic data were only available for 5/11 individuals depicted in this graph.

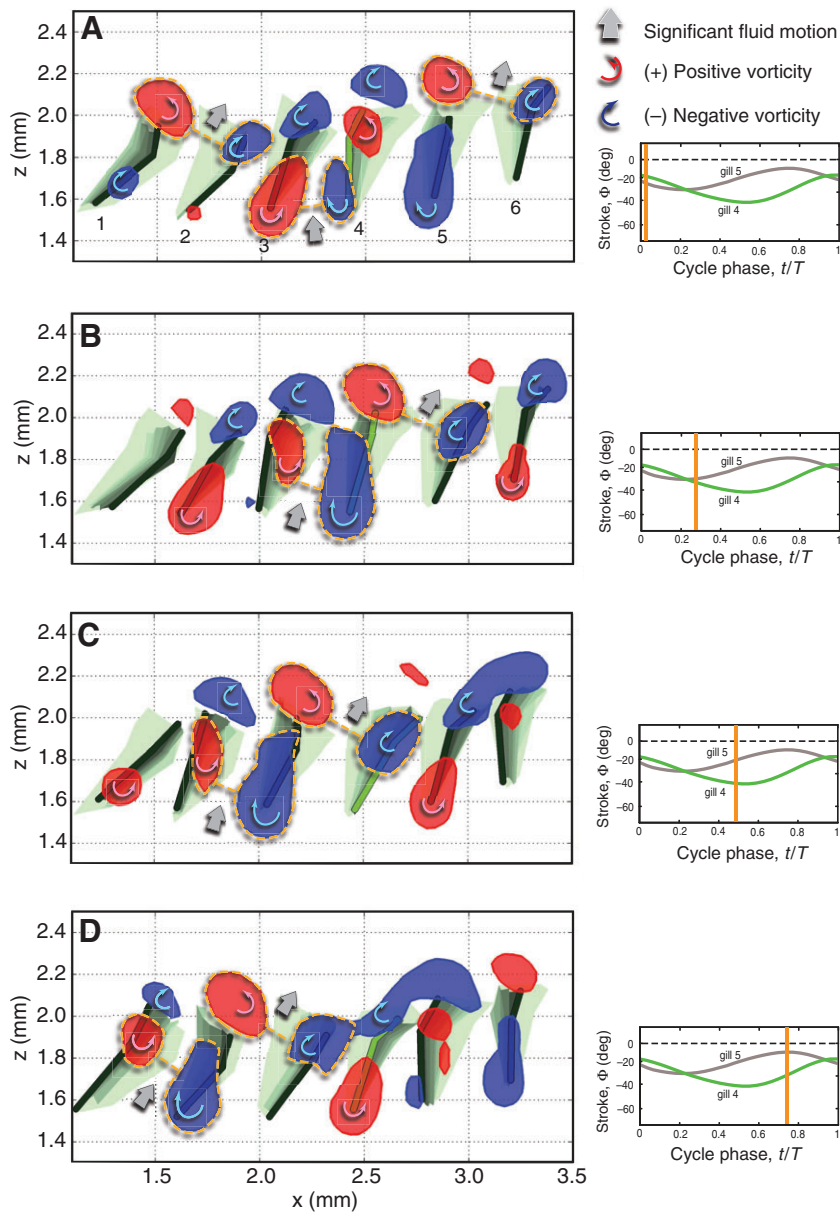


Fig. 10. Isocontours of positive (red) and negative (blue) vorticity for $Re=21.6$. Vortex outlines are based on the actual data. Gills are shown at each instant in the cycle as a black line (red for gill 4), with previous positions shown as gray shading, with darker tones indicating more recent positions. (A) Complete section ending at $t/T=1$; (B) slice depicting $t/T=0.07$; (C) slice depicting $t/T=0.31$; (D) slice depicting $t/T=0.52$; (E) slice depicting $t/T=0.75$. The panels on the right show the stroke position of gill 4 and 5, with a green bar indicating the phase of the cycle.

gill elements throughout the array is apparent. More specifically, the generation of the positive vorticity on the dorsal edge (DR+) corresponds to gill retraction, while the negative vorticity (DP-) corresponds to gill protraction. Examining the positioning of this vorticity and the resulting flow at different points of the cycle provides an explanation for how the net mean flow is generated (Fig. 10B–E). Starting just after gill 4 retraction (Fig. 10B), a vortex ring corresponding to the retraction phase has just formed on gill 4. Gill 3 is nearing its peak protraction velocity, creating a widening gap, and a vortex ring with opposite sign is already well formed as a result. The proximity of the opposite sign vorticity between the ventral regions of gills 3 and 4 forms a dipole with an induced velocity directed towards the widening gap, aiding the filling of the inter-gill region. Note that all of these vortices tend to exhibit distortions in their shape due to the local convection and diffusion of the vorticity as it is being generated; the ventral vortices are elongated along the surface of the gill because of the inflow from the ventral region, whereas the dorsal vortices are often elongated along the arc of the gill tip.

Simultaneous to the initiation of gill 4 retraction, gill 5 has just passed its peak retraction velocity and has a well formed DR+ and VR- vortex attached near and over its surface. The groupings DR5+/DP6- as well as DR4+/VR5- also form dipole pairs that induce flow in the dorsal-posterior direction. For the DR5+/DP6- vortex dipole, this induced flow is the ejection of fluid away from the dorsal aperture of the inter-gill space. For the DR4+/VR5- vortex dipole, this induced flow is the infilling of fluid into the inter-gill space through the ventral aperture. The phasing of the gill movements to produce these particular pairings is a common theme and appears to be key to the generation of the dorsally directed flow observed in the time-averaged velocity field. This theme is repeated at the quarter-cycle point (Fig. 10C, by DR3+/VR4- and more strongly by DR4+/DP5-), the half-cycle (Fig. 10D, by DR3+/DP4-) and the three-quarter cycle (Fig. 10E, DR2+/DP3-) points as the dorsal tips approach each other in neighboring gills, moving in a retrograde wave toward the anterior of the array. The generation of a net mean current by a specific arrangement of vorticity due to the

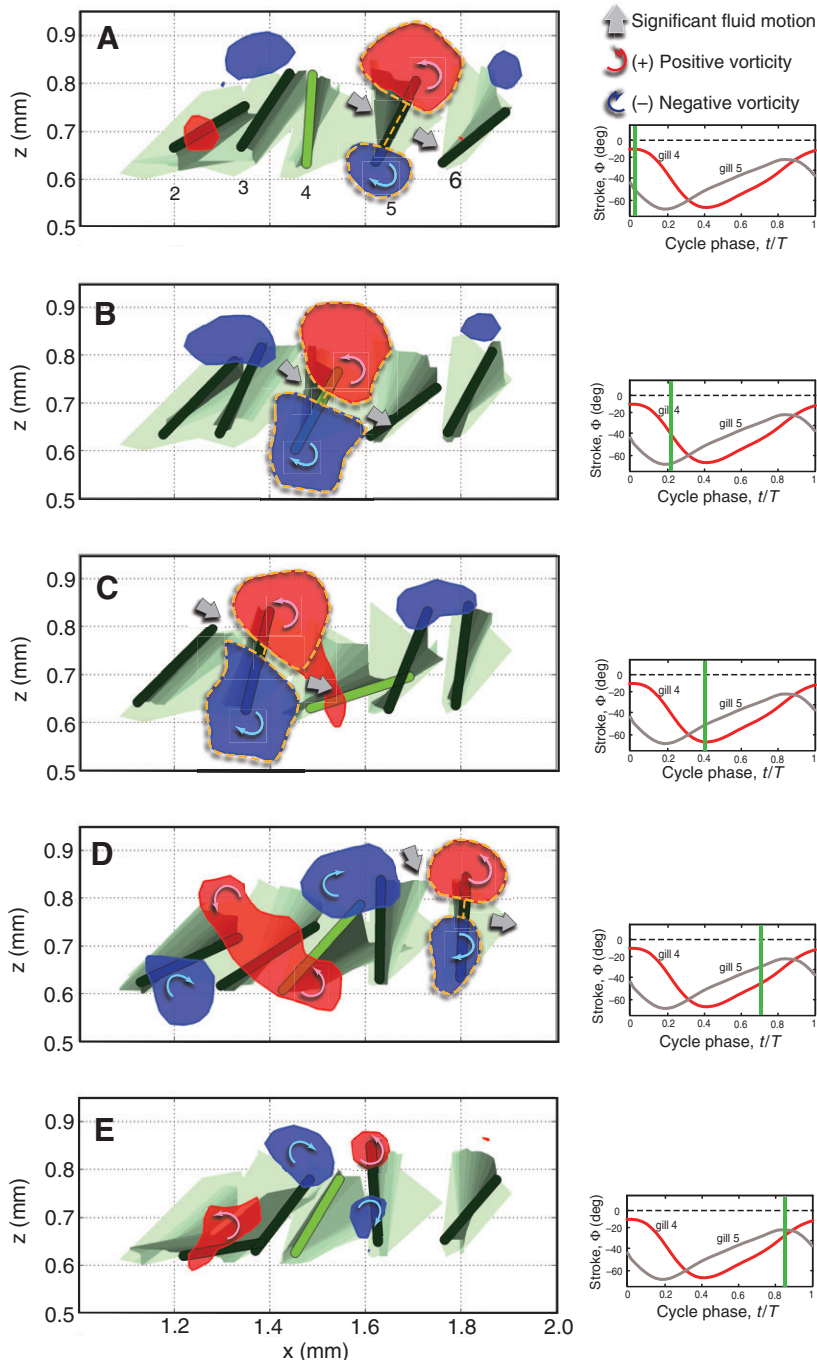


Fig. 11. Isocontours of positive (red) and negative (blue) vorticity for $Re_f=2.3$. Vortex outlines are based on the actual data. Gills are shown at each instant in the cycle as a black line (red for gill 4), with previous positions shown as gray shading, with darker tones indicating more recent positions. (A) Complete section ending at $t/T=1$; (B) slice depicting $t/T=0.04$; (C) slice depicting $t/T=0.2$; (D) slice depicting $t/T=0.4$; (E) slice depicting $t/T=0.69$; (F) slice depicting $t/T=0.86$. The panels on the right show the stroke position of gill 4 and 5, with a green bar indicating the phase of the cycle.

phased stroke kinematics of a serial appendage array can be thought of as a ‘phased vortex array’ pumping mechanism. This construct is useful for explaining the observed hydrodynamic operation for both the high and low Re conditions.

The low Re_f condition, $Re_f=2.1$, is shown in Fig. 11. Similar to the high Re_f case, the dorsal perspective reveals patterns of retraction-generated positive vorticity (DR+) moving in the posterior direction and a streak of protraction-generated negative vorticity (DP-) moving in the anterior direction (Fig. 11A). The size of the vortices are much larger relative to the inter-gill spaces, and much of the finer features of the vortex topology are lost because of the larger relative influence of diffusion. Aside from these general differences, the arrangement of the vorticity as a result of the stroke kinematics is also significantly altered. The most prominent difference is

phasing of the gills to produce a distinct and isolated ‘power’ stroke during the retraction phase of each gill. This is clearly visible in gills 5, 4 and 3 in Fig. 11, each of which has been captured close to the peak retraction velocity of the respective gill. This relatively isolated ‘power’ stroke in conjunction with the comparatively larger vortex size had the effect of making the dominant vortex interaction occur within the dipole pair of the ring itself (DR5+/VR5-, DR4+/VR4-, DR3+/VR3-), rather than with adjacent vortex structures produced by other gills. As a result, the predominant flow produced by this stroke corresponds to a flow through the center of the ring and in the direction of motion of the gill (ventral–posterior), which is entirely consistent with the inter-gill flux measurements presented in Fig. 7. The other difference that can be observed is that the increased stroke range combined with

the increased variation in pitch carries the positive dorsal retraction vortex (DR+) toward the ventral edge of the neighboring posterior gill, which soon starts its protraction (VP+), creating a continuation of the vortex (see, for example, DR3+ to VP4+ in Fig. 11D). The combination of the VP+ vortex with the formation of a much stronger negative dorsal vortex (DP-) on the same gill leads to a minor retrograde flow, i.e. anteriorly directed flow opposite to the full stroke cycle averaged mean flow at that location (see Fig. 11D). Finally, the last major difference is the coordinated protraction of several gills, as best exemplified by gills 3, 4 and 5 (Fig. 11E-F). Their combined motion diminishes the amount of circulation produced per gill, reducing the magnitude of the retrograde flow, as evidenced by the circulation p:r ratio (Fig. 6C) and comparison of the inter-gill flux exiting the inter-gill volume during these two events (Fig. 7A-C, time $t/T \sim 0.4-1$).

The timing and positioning of the vortices are key to producing the net dorsal flow at the high Re_f cases. At the low Re_f cases, the relatively larger vortices interfere with production of the ventral flow, resulting in a much weaker flow, due to cancellation of opposite-signed vorticity from cross diffusion. *C. triangulifer* exhibited a consistent flapping behavior when R_f was less than one half the gill length, corresponding to an $Re_f \sim 6$. Below this transition size, the phase vortex array pump reconfigures its topology in order to maintain effective pumping. Such a basic pumping mechanism would not extend down to arbitrarily small Re_f , as eventually diffusion would generate vortices larger than the array itself. In terms of vorticity manipulation for optimal thrust production or pumping efficiency, much recent work has focused on the formation of a vortex rings produced by a transient starting jet (Dabiri and Gharib, 2005; Gharib et al., 1998). In particular, Dabiri and Gharib (Dabiri and Gharib, 2005) indicated that diverse biological flows, such as those produced by mitral cardiac valves as well as squid funnel exits, follow an optimal scaling of $L/D \sim 4$, where L is the ejection distance of the vortex ring and starting jet, and D is the ring diameter. L/D is referred to as the formation number. For the mayfly, the vortex rings are not produced by a jet, but rather the stroke motion of the gills. An approximately equivalent formation number can be calculated taking the ejection length to be the stroke arc of the gill tip, $L = L_g \Delta\theta$, and the vortex ring diameter is approximately the size of the gill, $D \sim L_g$. Using these values (Table 1), the equivalent formation number is as large as 0.9 for the small nymphs, but shrinks to around 0.4 for the larger nymphs. This is also consistent with the circulation growth rates shown in Fig. 6, which show continual growth and decay without significant saturation, which would be expected once the critical formation number is reached. Such low values of the formation number is far from the optimum speculated for the general jetting cases, and speculatively extrapolated to flapping motions (Dabiri and Gharib, 2005). It would seem that the key elements of mutual interaction between adjacent plates are dominating the flow kinematics. This may be due to the restricted stroke range caused by the proximity of adjacent gills that precludes the possibility of reaching anywhere close to the optimal formation number.

This is the first study to resolve the flow structures within an oscillatory array, revealing fluid scaling that may explain previously quantified shifts in gill morphology and kinematics (Sensenig et al., 2009). All of these shifts probably serve to promote effective ventilation as animals grow through the intermediate Re range. The mechanism of pumping (phased-vortex array) was similar across the observed Re range, but its configuration was modified by the fact that vortex size was nearly the same for all growth stages because of the invariance of the gill-beat frequency. Therefore, this

may be a hydrodynamic feature that places a lower limit on effective operation of the more symmetric flapping mechanism observed in the largest nymphs. The question remains as to why the nymphs do not increase frequency at small body size so that 'flapping' could be used earlier in ontogeny. One may speculate several possible reasons why this is observed. First, rowing and flapping may be energetically optimal at the Re at which they are used by nymphs. Second, depending on metabolic rate and oxygen concentration, diffusion alone may be sufficient in supplying oxygen at small nymph sizes. Indeed, some of the youngest instars were never observed to actively use their gills. Therefore, under this hypothesis, the phased vortex array could be seen as primarily designed for the large nymph instars. Numerical simulations are currently underway to discriminate between these hypotheses. Regardless, the vortex diffusion distance, when available from fluid imaging, may prove to be a useful parameter in understanding the specific changes in behavior and function of diverse taxa.

LIST OF SYMBOLS AND ABBREVIATIONS

dA	the scalar differential area of the surface
D	dorsally directed jet
DP	dorsal protraction vortex
DR	dorsal retraction vortex
f	plate oscillation frequency
k	advance ratio L characteristic length of the appendage or moving body
L_a	animal length not including caudal filaments
L_g	gill total length
L_{is}	inter-gill spacing
L_{vd}	vortex diffusion distance
L_{rs}	gill root separation distance
LR	lateral retraction vortex
MP	medial protraction vortex
MR	medial retraction vortex
\mathbf{n}	unit normal vector for the surface of integration
R	reference length
Re	Reynolds number
Re_f	frequency Reynolds number
R_v	maximum vortex radius
T	stroke period
U	characteristic velocity
V	ventrally directed jet
\mathbf{v}	velocity vector
VP	ventral protraction vortex
VR	ventral retraction vortex
η	kinematic viscosity, $=\mu/\rho$
$\Delta\theta$	stroke arc angle
Δl	scalar incremental length along designated line for flux measurement
ΔQ	local flux
μ	dynamic viscosity
τ	fraction of a stroke period
Γ	circulation
ρ	density
ω	vorticity vector

ACKNOWLEDGEMENTS

We thank David Funk at the Stroud Water Research Center for supplying animals and the National Science Foundation (under grant CBET0730907). A.T.S. was supported by the Gahan Scholarship Fund. J.W.S. acknowledges the support of the Maryland Agriculture Experiment Station. The authors are also grateful to Prof. James Duncan, Department of Mechanical Engineering, University of Maryland, for the use of the high-speed camera equipment, and Prof. Charles Mitter, Department of Entomology, University of Maryland, for the use of the microscopes.

REFERENCES

- Borrell, B. J., Goldbogen, J. A. and Dudley, R. (2005). Aquatic wing flapping at low Reynolds numbers: swimming kinematics of the Antarctic pteropod, *Clione antarctica*. *J. Exp. Biol.* **208**, 2939-2949.

- Childress, S. and Dudley, R.** (2004). Transition from ciliary to flapping mode in a swimming mollusc: flapping flight as a bifurcation in Re_{ω} . *J. Fluid Mech.* **498**, 257-288.
- Dabiri, J. O. and Gharib, M.** (2005). The role of optimal vortex formation in biological fluid transport. *Proc. R. Soc. B: Biol. Sci.* **272**, 1557-1560.
- Drucker, E. G. and Lauder, G. V.** (1999). Locomotor forces on a swimming fish: three-dimensional vortex wake dynamics quantified using digital particle image velocimetry. *J. Exp. Biol.* **202**, 2393-2412.
- Ellington, C. P.** (1984). The aerodynamics of hovering insect flight. V. A vortex theory. *Phil. Trans. R. Soc. Lond. B, Biol. Sci.* **305**, 115-144.
- Funk, D. H., Jackson, J. K. and Sweeney, B. W.** (2006). Taxonomy and genetics of the parthenogenetic mayfly *Centroptilum triangulifer* and its sexual sister *Centroptilum alamance* (Ephemeroptera:Baetidae). *J. North Am. Benth. Soc.* **25**, 417-429.
- Gharib, M., Rambod, E. and Shariff, K.** (1998). A universal time scale for vortex ring formation. *J. Fluid Mech.* **360**, 121-140.
- Hunt, G., Park, L. E. and Labarbera, M.** (2007). A novel crustacean swimming stroke: coordinated four-paddled locomotion in the cypridoidean ostracode *Cypridopsis vidua* (Muller). *Biol. Bull.* **212**, 67-73.
- Jiang, H., Meneveau, C. and Osborn, T. R.** (2002). The flow field around a freely swimming copepod in steady motion. Part II: Numerical simulation. *J. Plankton Res.* **24**, 191-213.
- Kohlhage, K. and Yager, J.** (1994). An analysis of swimming in remipeded crustaceans. *Phil. Trans. R. Soc. Lond. B, Biol. Sci.* **346**, 213-221.
- Lent, C. M.** (1977). The mechanism for co-ordinating metachronal limb movements between joined male and female *Artemia salina* during precopulatory behaviour. *J. Exp. Biol.* **66**, 127-140.
- Malkiel, E., Sheng, J., Katz, J. and Strickler, J. R.** (2003). The three-dimensional flow field generated by a feeding calanoid copepod measured using digital holography. *J. Exp. Biol.* **206**, 3657-3666.
- Meinhart, C., Wereley, D. and Santiago, J.** (2000). A PIV algorithm for estimating time averaged velocity fields. *J. Fluids Eng.* **122**, 285-289.
- Olsen, M. G. and Adrian, R. J.** (2000). Out-of-focus effects on particle image visibility and correlation in microscopic particle image velocimetry. *Exp. Fluids* **29**, 166-174.
- Poelma, C., Dickson, W. and Dickinson, M.** (2006). Time-resolved reconstruction of the full velocity field around a dynamically-scaled flapping wing. *Exp. Fluids* **41**, 213-225.
- Rayner, J. M. V.** (1979). A new approach to animal flight mechanics. *J. Exp. Biol.* **80**, 17-54.
- Sensenig, A. T., Kiger, K. T. and Shultz, J. W.** (2009). The rowing-to-flapping transition: ontogenetic changes in gill-plate kinematics in the nymphal mayfly *Centroptilum triangulifer* (Ephemeroptera, Baetidae). *Biol. J. Linn. Soc.* **98**, 540-555.
- Spedding, G. R., Rosen, M. and Hedenstrom, A.** (2003). A family of vortex wakes generated by a thrush nightingale in free flight in a wind tunnel over its entire natural range of flight speeds. *J. Exp. Biol.* **206**, 2313-2344.
- van Duren, L. A. and Videler, J. J.** (2003). Escape from viscosity: the kinematics and hydrodynamics of copepod foraging and escape swimming. *J. Exp. Biol.* **206**, 269-279.
- Walker, J. A.** (2002). Functional morphology and virtual models: physical constraints on the design of oscillating wings, fins, legs, and feet at intermediate Reynolds numbers. *Integr. Comp. Biol.* **42**, 232-242.
- Williams, T. A.** (1994a). Locomotion in developing *Artemia* larvae: mechanical analysis of antennal propulsors based on large-scale physical models. *Biol. Bull.* **187**, 156-163.
- Williams, T. A.** (1994b). A model of rowing propulsion and the ontogeny of locomotion in *Artemia* larvae. *Biol. Bull.* **187**, 164-173.
- Wu, J.** (1981). Theory for aerodynamic force and moment in viscous flows. *AIAA J.* **19**, 432-441.
- Yen, J., Brown, J. and Webster, D. R.** (2003). Analysis of the flow field of the krill, *Euphausia pacifica*. *Mar. Fresh. Behav. Physiol.* **36**, 307-319.